

Aspherical lens shapes for focusing synchrotron beams

Manuel Sanchez del Rio^{a*} and Lucia Alianelli^b^aEuropean Synchrotron Radiation Facility, France, and ^bDiamond Light Source Ltd, UK.
E-mail: srio@esrf.eu

Aspherical surfaces required for focusing collimated and divergent synchrotron beams using a single refractive element (lens) are reviewed. The Cartesian oval, a lens shape that produces perfect point-to-point focusing for monochromatic radiation, is studied in the context of X-ray beamlines. Optical surfaces that approximate ideal shapes are compared. Results are supported by ray-tracing simulations. Elliptical lenses, rather than parabolic, are preferred for nano-focusing X-rays because of the higher peak and lower tails in the intensity distribution. Cartesian ovals will improve the gain when using high-demagnification lenses of high numerical aperture.

Keywords: X-ray lens; aspherical lens; aberrations; ray-tracing; Cartesian oval.

1. Introduction

X-ray beamlines that produce micrometre and submicrometre beams demand high-quality optical surfaces with extremely small manufacturing errors. With grazing-incidence optics (typically mirrors in meridional focusing), slope errors produce a smearing, s , of the spot, with $s = 2\sigma_{\text{slope}} q$. Here q is the distance of the optics (mirror) to the focal plane. Current slope errors for synchrotron mirrors are of order $\sigma_{\text{slope}} = 0.5 \mu\text{rad}$; therefore, using a typical focusing distance $q \simeq 0.1\text{--}0.5 \text{ m}$, the broadening due to slope errors only is about $0.1\text{--}0.5 \mu\text{m}$, certainly to be taken into consideration when submicrometre focusing is required. Some geometric aberrations can be eliminated by selecting a theoretical aberration-free surface. Co-axial optical systems like lenses, where the beam runs parallel to the optical axis, are much less affected by slope errors. Figure errors and aberrations are minimized by designing surface profiles as close as possible to the theoretical shape, which is aspheric in all cases. Spherical surfaces are easier to manufacture and may be produced with a high-quality polishing. They approximate the ideal aspherical shape and can be used when the degradation in the focal spot is acceptable, in particular for reflective optics. In addition to aberrations and effects of surface errors usually computed by geometrical optics, every optic produces a diffraction broadening of the order of λ/NA (λ is the wavelength and NA is the numerical aperture). Lenses with high NA minimize the diffraction broadening, but are more sensitive to the geometrical aberrations, thus there is an interest in studying the limits of geometrical focusing for nanofocus beamlines. The demagnification of current synchrotron sources (typical sizes of $10 \mu\text{m}$ or larger) into nano-sized spots requires efficient optical systems that take into account a non-trivial combination of surface errors, diffraction effects and source char-

acteristics; conserving the beam emittance with a very high demagnification optical system is a complex task.

Although the first observation of X-ray refraction was made in 1916 (Barkla, 1916), X-ray refractive lenses are relatively recent devices developed thanks to the advent of third-generation synchrotron sources. They gained popularity over recent decades for making X-ray micro- and nano-probes (focusing), collimating synchrotron beams, as well as for imaging applications. In 1991, Suehiro *et al.* (1991) first proposed the potential benefits of X-ray lenses in the context of third-generation synchrotron sources, suggesting advantages of lenses over X-ray mirrors in terms of reduced optics size, less sensitivity to surface errors and higher stability. In 1996, Snigirev *et al.* (1996) fabricated the first compound lenses by drilling arrays of cylindrical holes in aluminium. They demonstrated the ability of this device to focus X-rays down to $8 \mu\text{m}$, opening the door to the development and popularization of a new collection of refracting devices. They also suggested the use of lithographic methods for fabricating parabolic-shaped lenses. Soon after, lens arrays of parabolic profiles were fabricated using drilling and pressing techniques and used for focusing and imaging applications (Lengeler, Schroer, Tummler *et al.*, 1999; Lengeler, Schroer, Richwin *et al.*, 1999; Lengeler *et al.*, 1998). Rapid advancements in micro-fabrication technology have now allowed fabrication of step-shape planar lenses made of parabolic arrays (Aristov *et al.*, 2000). Evans-Lutterodt *et al.* (2003) built a compound lens based on elliptical profiles and pointed out that the ellipse is the ideal profile for focusing a collimated beam to a point. The smaller spot size in a standard lens is limited by the size of the Airy disc, which is proportional to λ/NA . However, the accepted NA is limited by total reflection on the lens surface. This limitation can be overcome: Evans-Lutterodt *et al.* (2007) demonstrated that kinoform lenses are not limited by the

critical angle, and Schroer & Lengeler (2005) proposed an adiabatically focusing lens, an array of lenses with increasing curvature from the entrance to the exit lens. Two-dimensional focusing to ~ 50 nm was already achieved in 2005 (Schroer *et al.*, 2005) using arrays of focusing lenses. Arrays of kinoform lenses have to be used to achieve ultra-short focal lengths (Evans-Lutterodt *et al.*, 2007). Parabolic and elliptic lenses greatly reduce spherical aberrations. Chromatic aberrations are always present, as they are intrinsic to refractive lenses.

Despite the existence of a vast literature on spherical and parabolic compound refractive lenses, there is no clear discussion on why one should prefer one shape over the other, except for the case of single elliptical lenses (Evans-Lutterodt *et al.*, 2003). The theoretical lens shape to perform a point-to-point focus is neither elliptical or parabolic. This old result, known for centuries, has not been discussed in the context of micro- and nanofocusing X-rays, with the possible exception of Evans-Lutterodt *et al.* (2007) who used optics in which the ‘figure of each lens was deduced from Fermat’s theorem’. Shaping the lens to perform perfect point-to-point focusing gives, at least in theory, a chance to further reduce the focal spot.

The process of designing a lens-based optical instrument is often assisted by ray-tracing simulations. We thus performed ray-tracing and computational experiments using the *SHADOW* package (Cerrina & Sanchez del Rio, 2010), well known by the synchrotron radiation community. In this paper we present a theoretical discussion supported by computer modelling on the effect of ideal and approximated surfaces to focus beams. Computer experiments allow studies of lenses with different shapes under strictly the same conditions, a situation that is very difficult to reproduce experimentally. It is important to quantitatively evaluate the effects of different lens shape in a wider context, also including other focal broadening effects owing to slope error and diffraction. The ultimate limit of X-ray focusing has been discussed in relation to diffraction (Evans-Lutterodt *et al.*, 2007; Schroer & Lengeler, 2005), and this work addresses the geometrical limits due to surface shape. The different aspects of focusing X-rays with lenses calculated using *SHADOW* aim to (i) benchmark the code for some simple cases well known from the optics textbooks, (ii) extend the applicability of the code to other cases that are not easily analyzed analytically, and (iii) present the usability of this code for lens simulations to the synchrotron community.

2. Fermat’s principle and its consequences: Snell’s law, focusing radius and surface shape

Most of the fundamental equations used in this paper can be derived from Fermat’s principle. The optical path OP for going from a point P_1 to another P_2 is defined as

$$OP = \int_{P_1}^{P_2} n \, ds, \quad (1)$$

where n is the refraction index of the media and the integral is along the trajectory.

Fermat’s principle, or the principle of least time, discovered by Pierre de Fermat in ~ 1650 , states that light travels from P_1 to P_2 through a trajectory that makes OP an extremum, *i.e.* $\delta(OP) = 0$. It follows that (Feynman, 1963, p. 26-7) a ray travelling in a particular path has the property that, if we make a small change in the ray in any manner whatever, for example in the location at which it arrives at the mirror, or the shape of the curve, or anything, then there will be no first-order change in the OP; there will only be a second-order change in the time.

The first equation to be derived from Fermat’s principle is the law governing the refraction at a plane interface (see Appendix A1). Known as Snell’s laws in honour of Willebrord Snellius, it was also published by René Descartes. Whether the works of Snellius and Descartes were independent or whether Descartes had access to unpublished material (or a book destroyed by fire) is still under debate. The first antecedent of Snell’s laws can be found in the work of Claudius Ptolemy of Alexandria, who made tables with ~ 140 angles of refraction of light in three media: air, glass and water (see, for example, Feynman, 1963, pp. 26-2). These tables were published by Vitellius in his ten volumes of *Handbook of Optics*. The Persian physicist Ibn Sahl wrote a textbook in 984 where he explained how curved mirrors and lenses bend and focus light. He was probably the discoverer of the law of refraction (Rashed, 1990; Zghal *et al.*, 2007).

Snell’s law states that the change in the direction of light at the interface that separates two media of refraction indices n_1 and n_2 is given by

$$n_1 \sin \theta_1 = n_2 \sin \theta_2, \quad (2)$$

where θ_1 (θ_2) is the incident (refracted) angle measured with respect to the surface normal. For ray-tracing purposes, it is more convenient to write Snell’s law in vector form (Herzberger, 1958, pp. 8–10),

$$n_1(\mathbf{v}_1 \times \mathbf{n}) = n_2(\mathbf{v}_2 \times \mathbf{n}), \quad (3)$$

where \mathbf{v}_1 (\mathbf{v}_2) is a unitary incident (refracted) vector and \mathbf{n} is the normal to the surface. In practice, one calculates \mathbf{v}_2 as a function of known \mathbf{v}_1 and \mathbf{n} ,

$$n_2 \mathbf{v}_2 = n_1 \mathbf{v}_1 + \Gamma \mathbf{n}, \quad (4)$$

where Γ , known as the astigmatic constant, or deviation constant, is given by

$$\Gamma = +[n_2^2 - n_1^2 + (\mathbf{v}_1 \cdot \mathbf{n})^2]^{1/2} - n_1(\mathbf{v}_1 \cdot \mathbf{n}). \quad (5)$$

A phenomenon discovered by Kepler appears when $n_1 > n_2$ for incident angles larger than the critical angle θ_c . Here, $\theta_c = \arcsin(n_2/n_1 \sin \theta_2) > \arcsin(n_2/n_1)$, so there is no solution to Snell’s law, and the ray is not refracted but totally reflected. When performing ray tracing, there is no real solution of equation (2); therefore the ray is removed from the beam. The refraction index of the media depends on the incident wave energy. This implies that refractive lenses have chromatic aberrations, as light rays of different energies are deviated

differently at the surface. The real part of the refraction index is larger than unity for visible light ($n > 1$) and less than unity for X-rays ($n < 1$). Absorption is generally included through the imaginary part of the refraction index and is not considered here. A single lens has two interfaces, and a compound lens is an array of simple lenses with a common optical axis.

When the interface separating the two media is curved, the light may be focused. The simplest interface surface is a sphere. Using Fermat's principle one can calculate the radius of curvature R to focus a beam coming from a point at p from the lens on the optical axis to another point at q also on the optical axis (see Appendix A2). It is given by

$$(n_1/p) + (n_2/q) = (n_2 - n_1)/R. \quad (6)$$

This equation is valid when the angles between the rays and the optical axis are small, *i.e.* for paraxial rays or small numerical apertures.

Fermat's principle can be used to obtain the ideal surface shape that produces point-to-point focus. The surface obtained in this way is called a Cartesian oval (Fig. 1), and was introduced by Descartes in *La Geometrie* (Descartes, 1637), an appendix of the 'Discours de la Méthode'. For a commented facsimile version, see Debart (2011).

The Cartesian oval is a particular case of the bi-circular quartic equation. Its derivation from Fermat's principle can be found in Appendix A3.

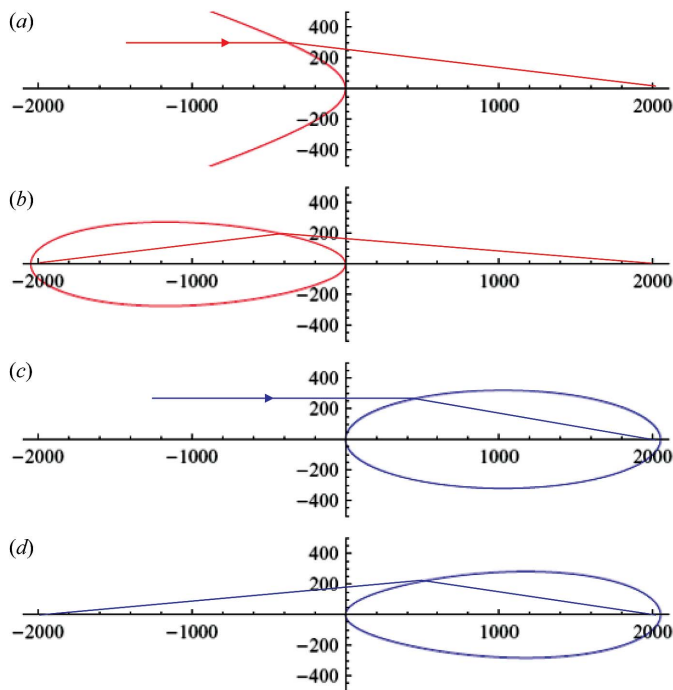


Figure 1 Illustration of refraction from a single interface separating two media with refraction indices n_1 and n_2 . (a) A hyperbola focusing a parallel beam travelling in a medium with $n_1 > n_2$. (b) A Cartesian oval focusing a divergent beam travelling in a medium with $n_1 > n_2$. (c) An ellipse focusing a parallel beam travelling in a medium with $n_1 < n_2$. (d) A Cartesian oval focusing a divergent beam travelling in a medium with $n_1 < n_2$.

3. Lens shape to focus collimated beams

When a source of size h is at infinity (zero divergence), the Cartesian oval degenerates into a conic surface (Lunenburg, 1964, p. 132) (Fig. 1),

$$(z - z_c)^2/a^2 \pm (x^2 + y^2)/b^2 = 1, \quad (7)$$

representing an ellipsoid or hyperboloid depending on the plus or minus sign, respectively, with cylindrical symmetry around z . The positions of the image (focal position) z_c and the semi-axes a and b are given by

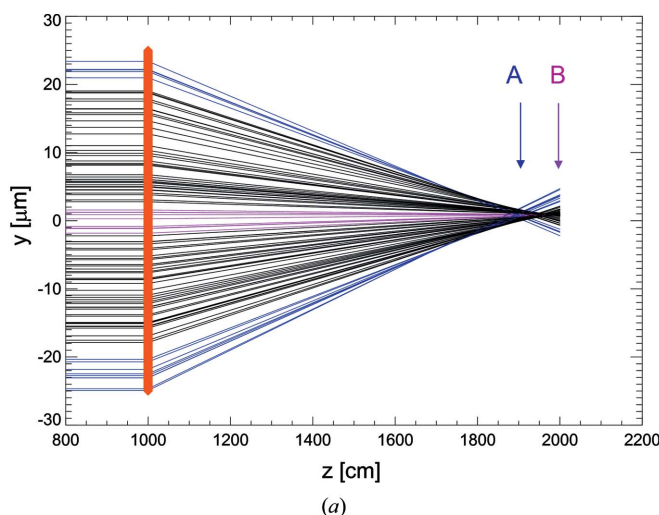
$$\begin{aligned} z_c &= qn_2/(n_1 + n_2), \\ a &= z_c, \\ b &= q[(|n_1 - n_2|)/(n_1 + n_2)]^{1/2}. \end{aligned} \quad (8)$$

The eccentricity e of the ellipse or hyperbola is

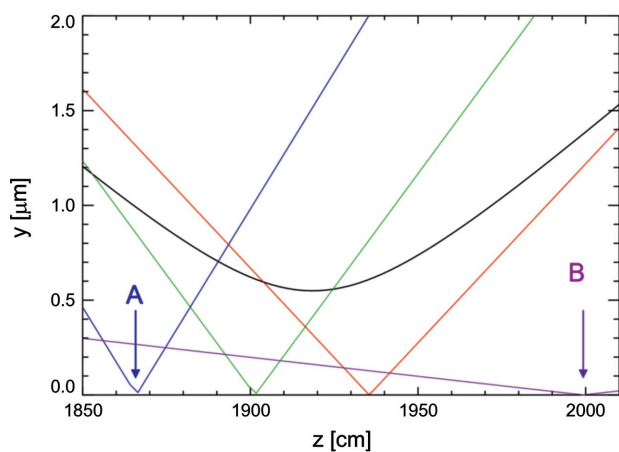
$$e = (a^2 \mp b^2)^{1/2} = q[n_1/(n_1 + n_2)]^{1/2}. \quad (9)$$

The ellipsoid is obtained when $n_1 < n_2$ (*e.g.* when X-rays go from a media $n_1 < 1$ to vacuum $n_2 = 1$) and the hyperboloid when $n_1 > n_2$ (*e.g.* visible light going from glass to vacuum). The former case, regarding the use of elliptic lenses for focusing collimated X-ray beams, has already been discussed in the literature (Evans-Lutterodt *et al.*, 2003). The latter case is the well known result that a hyperbolic concave lens transforms a plane wave into a spherical wave, and *vice versa* (Hecht, 1987).

A first ray-tracing simulation features a single focusing interface separating a lens medium (refraction index $n_1 \neq 1$) and vacuum ($n_2 = 1$) (Fig. 2). For simplicity only the YZ plane is displayed. Setting $p = -\infty$, $q = 1000$ cm and $n_1 = 0.999995$ (10 keV X-rays in silicon) in equation (6), we found that a spherical optical surface with $R = -50$ μm (*i.e.* convex) focuses the beam close to the desired focal position. Fig. 2(a) shows the ray-tracing results for a lens of diameter $h = 50$ μm . It illustrates the focusing of the paraxial rays (almost parallel to the optical axis illuminating the centre of the lens) and the marginal rays (arriving at the lens edge) and the formation of a caustic (the envelope of all refracted rays). Fig. 2(b) shows the evolution of beam size r.m.s. (root mean square) around the focal position. It illustrates how the best focus, defined as the one with the smaller r.m.s., is found in between the paraxial and marginal foci. The paraxial focus is found at q and the marginal focus somewhere upstream, at $q - \text{LSP}$, where LSP is the longitudinal spherical aberration (LPS = 133.95 ± 0.02 cm in our case). Primary aberration theory (Mahajan, 1998, p. 214) shows that the circle of least confusion (the one with smaller limits) is found at $q - 0.75$ LSP, and can be obtained by tracing the rays that hit the lens at heights $h' = \pm 0.866(h/2)$. The point with zero wavefront deviation at the edge is found at $q - 0.5$ LSP and corresponds to a trace of rays that hit the lens at heights $h' = \pm 0.707(h/2)$. These rays are also represented in Fig. 2(b). Finally, the theoretical minimum r.m.s. radius is at $q - 0.67$ LSP. The best focus (that minimizes the spot r.m.s.) from ray tracing is found at $q - (81.43 \pm 0.11 \text{ cm}) = (0.61 \pm 0.01)$ LSP. Spherical lenses have three important disadvan-



(a)



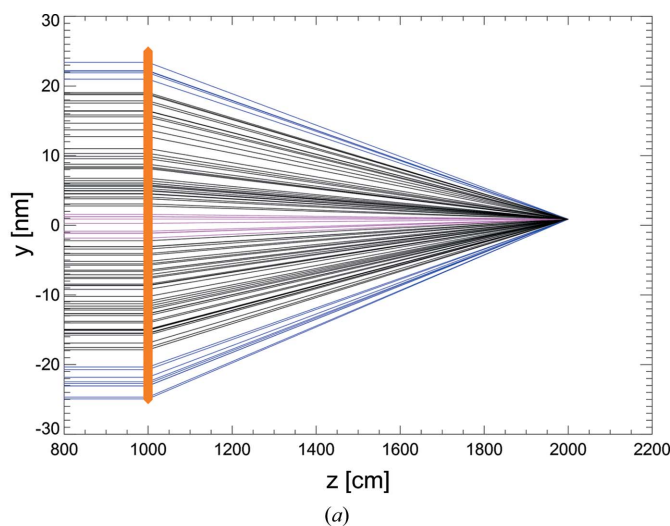
(b)

Figure 2

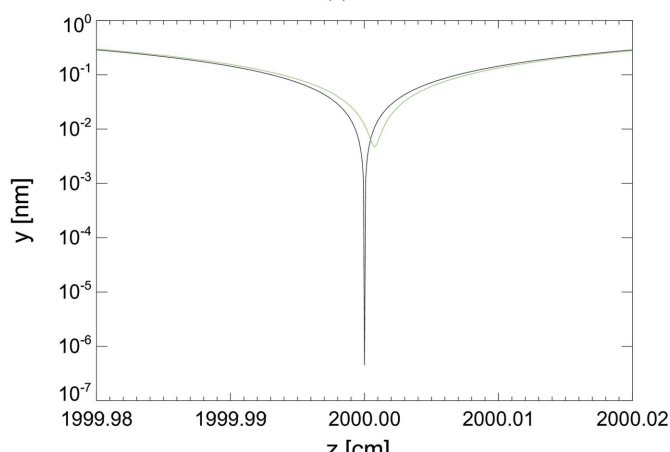
(a) Ray-tracing illustration of focusing a collimated incident beam using a single spherical surface. The focal distance is $F = 1000$ cm and the lens diameter is $h = 50$ μm . Marginal rays (blue) are focused at A and paraxial rays (magenta) at B. (b) Evolution of the beam dimension (r.m.s.) for the full beam (black), marginal rays (blue), paraxial rays (magenta), rays at height $h' = \pm 0.866(h/2)$ (green) and rays at height $h' = \pm 0.707(h/2)$ (red).

tages: (i) large broadening of the focal spot, (ii) defocus or shift of the ‘best’ focal position, and (iii) reduced acceptance because the lens cannot be larger than $2R$. Because of this, X-ray spherical lenses are no longer used.

Fig. 3(a) shows rays focused by an elliptical interface with semi-axes calculated using equation (8): $a = 500.00125$ cm and $b = 1.58204$ cm. When comparing with reflective optics, paraboloidal mirrors are used to focus collimated beams into a point, but this conic shape is not the ideal shape when using refractive optics. However, it is clear that a parabola approximates much better an ellipse or a hyperbola than the circle, therefore it is expected that aberrations can be drastically reduced, although not completely eliminated, using parabolas. In fact, using a parabola with equation $y^2 \pm 2Rz = 0$, where R is obtained from (6), we obtained a graph indistinguishable from the ellipse case of Fig. 3(a). To observe some (small) differences, the evolution of the beam dimension using an ellipse and a parabola are compared in Fig. 3(b). The results, shown on a logarithmic scale, show differences in spot



(a)



(b)

Figure 3

(a) Ray-tracing illustration of focusing a collimated incident beam using an elliptical surface. The focal distance is $F = 1000$ cm and the lens diameter is 50 μm . All rays, including paraxial (magenta) and marginal (blue), are focused at the same position. (b) Evolution of the beam dimension (r.m.s.) for the elliptical interface (black) and an approximated parabolic interface (green).

size only at the subnanometre level. A very small defocus is produced by the parabolic lens (see Fig. 3b) (the best focus r.m.s. is found at ~ 10 μm downstream from the paraxial focus).

In summary (see Fig. 4), it has been checked that a convex lens is needed for focusing X-rays ($n < 1$). Spherical shapes produce strong aberrations, and elliptic interfaces focus ideally collimated X-ray beams. In parallel, hyperbolic concave-shaped lenses focus collimated visible beams. On the other hand, converging X-ray beams are collimated by hyperbolic lenses whereas visible beams are collimated by elliptical lenses.

4. Numeric experiments using the Cartesian oval and its approximations

The reduction of the Cartesian oval (Appendix A3) to its explicit form $z(y)$ allows the lens profile to be described, but this analytical solution is rather cumbersome. Numerical

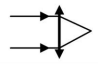
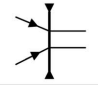
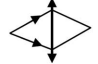
| | $n_1 < n_2$ | $n_1 > n_2$ |
|---|----------------|----------------|
| Collimated to convergent  | Ellipse | Hyperbola |
| Convergent to collimated  | Hyperbola | Ellipse |
| Divergent to convergent  | Cartesian oval | Cartesian oval |

Figure 4
Ideal surface shape for different focusing conditions.

solution of the fourth-degree equation (thus the numerical lens profile) has been calculated using *Mathematica* (<http://www.wolfram.com/>), and this profile has been used for creating a rotationally symmetric interface for *SHADOW* by means of the ‘presurface’ tool. Fig. 5 shows the performance of a Cartesian oval as compared with a paraboloidal lens. To stress the differences, the parameters have been chosen for a strong focusing, $p = 4700$ cm, $q = 10$ cm using $n_1 = 0.99999231$ (Si at 8 keV). The figure shows the r.m.s. spot size *versus* the lens diameter up to $h = 200$ μm diameter (lens length $L = 6$ mm) for an ideal point source. As expected, the Cartesian oval gives a point spot (within statistical, numerical and interpolation errors), whereas the paraboloid produces a broader spot that increases with lens diameter. In this configuration the paraboloid shows a non-negligible defocus, shifting the focal point to 8.4 mm downstream from the paraxial focus. It is found that the focal size can be reduced by about 70% by moving the detector plane to the best focus (dashed line), but still shows focusing aberrations compared with the Cartesian oval. Therefore, it is confirmed that the Cartesian oval performs optimally at high NA, under conditions where the paraboloid shows aberrations.

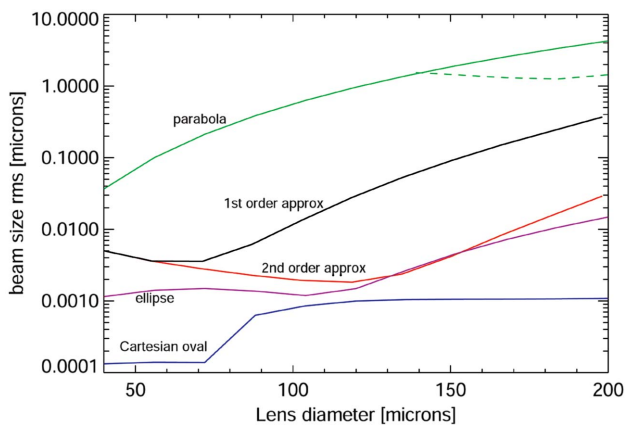


Figure 5
Focal spot size r.m.s. *versus* lens aperture for point-to-point focusing using an interface surface matching: parabola (green solid), parabola with defocus correction (green dashed), optimized first- (black) and second-order (red) profiles, ellipse (magenta) and Cartesian oval (blue).

For practical purposes, an aberration-free aspheric surface similar to the ideal surface can be calculated by adding a correction to an initial spherical or flat surface. Defining (as in *SHADOW*) a three-dimensional reference system centred at the optical element pole, with the y and x axes tangential to the lens surface at the lens centre, and the z axis along the optical axis, the foci are at $(0, 0, p)$ and $(0, 0, -q)$; the optical surface is defined as a mesh of z points on a grid in (x, y) ,

$$z_{ij} = z(x_i, y_j). \tag{10}$$

By defining a functional ‘optical path difference’ OPD between a ray passing through a generic point of the surface $P(x, y, z)$ (distant l_1 and l_2 from source and image point, respectively) and another ray passing through the lens centre, as

$$\begin{aligned} \text{OPD} &= l_1 n_1 + l_2 n_2 - (|p|n_1 + |q|n_2) \\ &= n_1 [x^2 + y^2 + (z - p)^2]^{1/2} + n_2 [x^2 + y^2 + (z + q)^2]^{1/2} \\ &\quad - (pn_1 + qn_2), \end{aligned} \tag{11}$$

it becomes obvious that OPD is zero for the (x, y, z) points belonging to the Cartesian oval.

Expanding OPD in a power series up to the second degree in z , we obtain

$$\begin{aligned} \text{OPD} &= -n_1 p - n_2 q + n_1 (p^2 + x^2 + y^2)^{1/2} \\ &\quad + n_2 (q^2 + x^2 + y^2)^{1/2} \\ &\quad + \left[-\frac{n_1 p}{(p^2 + x^2 + y^2)^{1/2}} + \frac{n_2 q}{(q^2 + x^2 + y^2)^{1/2}} \right] z \\ &\quad + \frac{1}{2} \left[\frac{n_1 (x^2 + y^2)}{(p^2 + x^2 + y^2)^{3/2}} + \frac{n_2 (x^2 + y^2)}{(q^2 + x^2 + y^2)^{3/2}} \right] z^2 \\ &\quad + O(z^3). \end{aligned} \tag{12}$$

By solving the equation $\text{OPD} = 0$, a second-degree equation on z for each (x_i, y_j) point in the grid, one immediately obtains the profile mesh $z(x, y)$. Numeric profiles created in first and second approximations have been introduced in *SHADOW* for ray tracing. Fig. 5 also includes the focal size results for these first and second approximation surfaces, as well as for the ellipsoid. It is noticeable that a first-degree expansion in OPD is sufficient to reduce the aberrations from the paraboloid, and a second-order correction gives a very good approximation to the Cartesian oval. The ellipsoid results are better than the second approximation. The approximated surfaces (first and second order) and ellipsoid do not present appreciable defocus. The differences between the ellipsoid and the paraboloid are not so important, and even not noticeable, when the lens demagnification is not so high, as will be discussed later.

5. Application of an aspherical lens to microfocus and nanofocus beamlines

Having discussed the ideal surface shapes and their approximations for a single X-ray lens, we present several examples of systems approaching real synchrotron radiation cases,

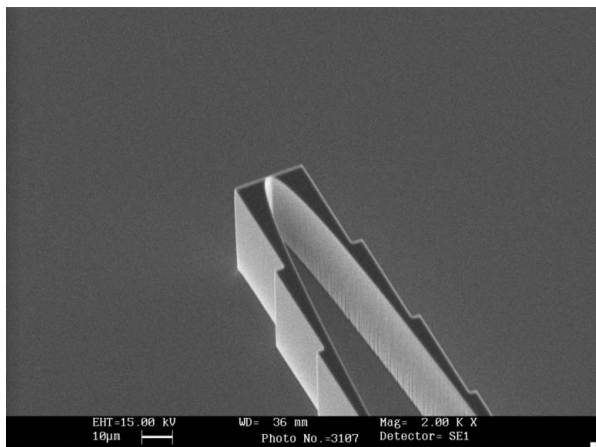


Figure 6
Scanning electron microscope image of a microfocusing single-element elliptical lens with a kinoform profile.

including the effect of the finite source size. A source matching the parameters of a diamond undulator at a photon energy $E = 8$ keV has been simulated by using Gaussian distributions ($\sigma_x = 12.3 \mu\text{m}$, $\sigma_y = 7 \mu\text{m}$, $\sigma_x' = 25 \mu\text{rad}$ and $\sigma_y' = 8 \mu\text{rad}$, X is in the horizontal plane and Y in vertical). The source–lens distance is $p = 47$ m, and three lens–image distances will be used for increasing the demagnification $M = p/q$. The non-absorbing lens is a good approximation for a kinoform lens (Alianelli *et al.*, 2009), of which an example is shown in Fig. 6. Cylindrical silicon lenses are considered (refraction index $n_1 = 0.99999231$), focusing only in the Z (vertical) plane.

Fig. 7 shows the simulated focal size *versus* lens diameter for the case where $q = 100$ cm ($M = 47$) for different lens shapes. In the parabolic case the aberrations appear at a lens diameter of $h \simeq 0.2$ mm, where the focal blurring is dominated by diffraction. When increasing the lens diameter or NA, the diffraction reduces, and above a diameter of $h = 0.55$ mm the

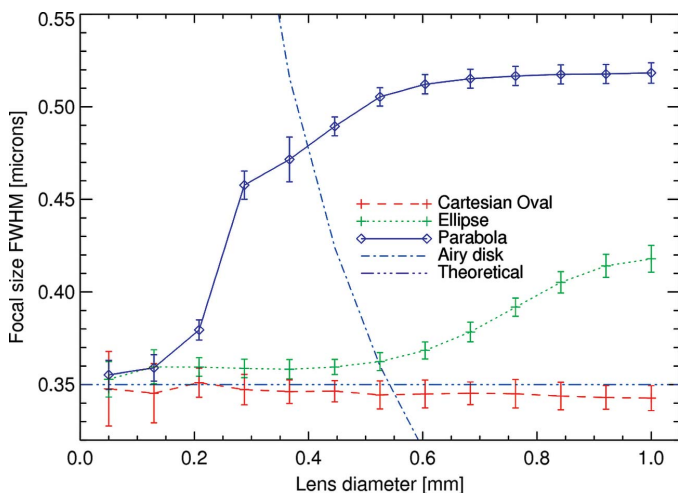


Figure 7
Simulations of focal spot *versus* lens diameter for parabolic and elliptical shapes. The source is a typical diamond undulator at $E = 8$ keV (approximated with a Gaussian source of $\sigma_y = 7 \mu\text{m}$, $\sigma_y' = 8 \mu\text{rad}$). The theoretical broadening owing to diffraction (an Airy disk of $1.22\lambda q/h$) is also shown, as well as the theoretical spot size ($2.35\sigma_y q/p$).

parabolic shape produces an almost constant spot of $\sim 0.5 \mu\text{m}$, whereas the ellipse produces a smaller focus ($0.34\text{--}0.42 \mu\text{m}$), and the Cartesian oval gives the theoretical value ($0.35 \mu\text{m}$).

Fig. 8 shows the intensity distribution of the focal spot for two different demagnifications M . The first case is representative of a microfocus beamline and considers a distance $q = 30$ cm, thus using a demagnification $M = 157$ and a theoretical focal size of 105 nm full width at half-maximum (FWHM). Fig. 8(a) shows the results for the small lens aperture ($h = 0.3$ mm, lens length $L \simeq 5$ mm). All lens shapes give a spot FWHM close to the theoretical one (101 ± 4 , 102 ± 6 and 131 ± 13 nm for the oval, ellipse and parabola, respectively). Both the Cartesian oval and the ellipse produce a spot with Gaussian shape, but the parabola spot distribution is not Gaussian and includes high tails. The appreciable increase of the tails produces a reduction of the peak intensity, decreasing the gain. Fig. 8(b) shows the same case for a lens with a larger aperture ($h = 0.5$ mm, $L \simeq 14$ mm). The FWHM are 105 ± 4 , 113 ± 6 and 121 ± 13 nm for the oval, ellipse and parabola, respectively. Here the focal spot owing to the ellipse is slightly degraded; some tails appear near the main peak, thus removing some intensity from the peak, but they go quickly to zero. The focus given by the parabola includes long tails with lower peak value, but the FWHM is not far from the ideal value. The Cartesian oval and elliptical lenses do not show appreciable defocus. The best r.m.s. focus by the parabola is found ~ 13 mm downstream of the paraxial focus. Interestingly, the focal FWHM is not improved by correcting the focal position by the r.m.s. defocus. On the contrary, it is highly enlarged, and the best focus obtained by minimizing the FWHM is found practically at the paraxial focal position. The aberrations become more important with increasing lens aperture both in the parabolic case and elliptic case. By reducing the source size by a factor of two we found that the tails are not reduced, even though the FWHM reduces and the peak increases accordingly. These calculations show that in some cases elliptical profiles are preferred to the parabolic ones because the ellipse approximates better the ideal Cartesian oval lens. The synchrotron beam is seen by the lens as a mostly collimated beam, as demonstrated by the indistinguishable elliptical lens profile (ideal for focusing a collimated beam) and the Cartesian oval (for point-to-point focusing) for the small lens aperture. This is valid for microfocusing or submicrofocusing lenses.

The last simulation matches a nanofocusing lens configuration with higher demagnification: focal positions $p = 47$ m, $q = 10$ cm. Here, $M = 470$ and the ideal focus is 35 nm. Fig. 8(c) shows that for a small aperture $h = 0.3$ mm ($L \simeq 12$ mm) the focal spot widths given by the three lens shapes are similar (30 ± 1 nm, 40 ± 2 nm and 38 ± 3 nm for the oval, ellipse and parabola, respectively), but the only one that does not present tails and fits satisfactorily with a Gaussian is the Cartesian oval. The tails extend to a distance of about 200 nm from the peak position for the elliptical lens. The largest possible lens aperture for the ellipse and the oval is $h = 0.4$ mm ($L \simeq 40$ mm), and the results are similar (Fig. 8d), but with longer tails. The depth of focus (defined as the depth where the waist

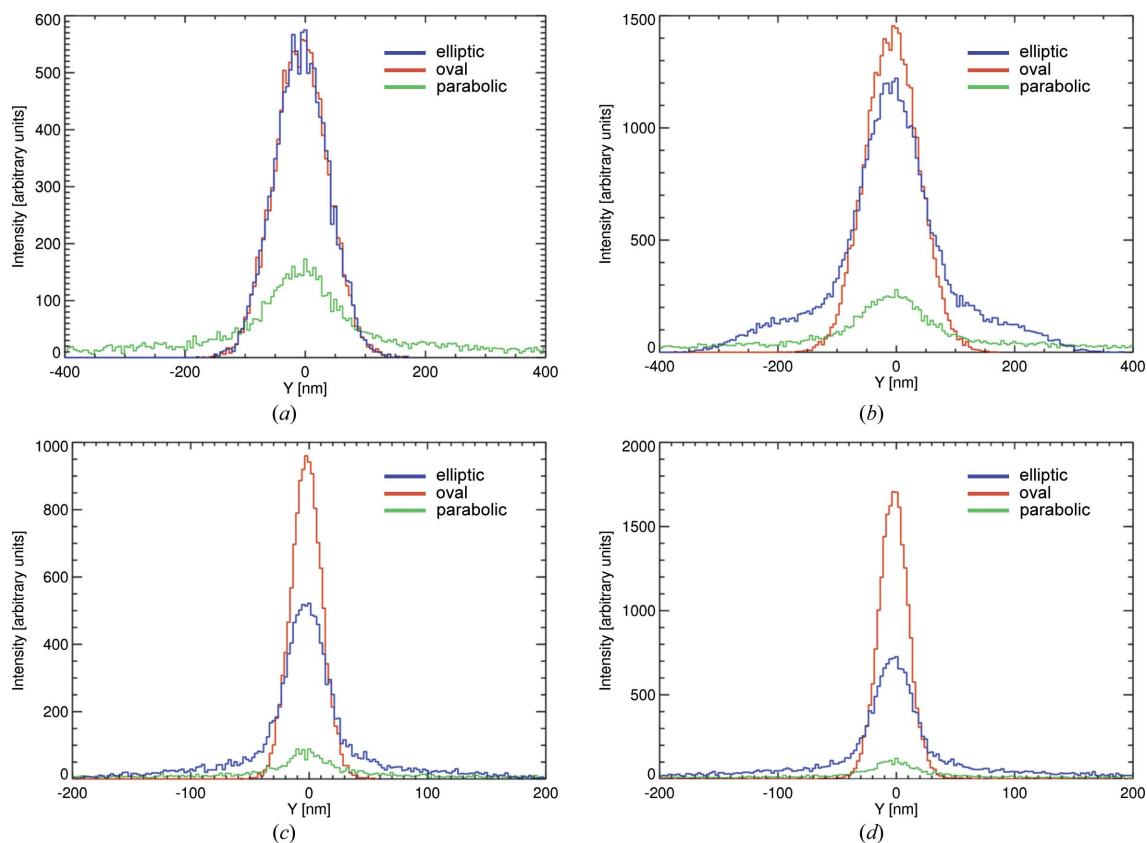


Figure 8 Simulation of vertical focusing using a single-element refractive lens at $p = 47$ m from the source. The diamond source size and divergence have been used, *i.e.* $\sigma_y = 7 \mu\text{m}$ and $\sigma_z = 8 \mu\text{rad}$. The figures show the intensity distribution at the focal plane given under the same illumination conditions, using Cartesian oval (red), elliptic (blue) and parabolic (green) lenses. The following cases are presented: (a) lens–image distance $q = 30$ cm, lens diameter $h = 0.3$ mm, (b) $q = 30$ cm, $h = 0.5$ mm, (c) $q = 10$ cm, $h = 0.3$ mm, and (d) $q = 10$ cm, $h = 0.4$ mm.

size increases by 25%) is about $250 \mu\text{m}$ for the parabolic lens, about $45 \mu\text{m}$ for the ellipse and $10 \mu\text{m}$ for the Cartesian oval.

These calculations show that the elliptical lenses approximate better the ideal Cartesian oval than parabolas and present less aberrations. However, it is remarkable that parabolic lenses also give good spot width values (FWHM) in good agreement with the experimental results for parabolic lenses reported in the literature.

6. Summary and conclusions

Numeric experiments have been carried out for focusing X-rays by a refracting interface with different shapes: Cartesian oval (the generic lens shape for point-to-point focusing), ellipse (ideal for focusing collimated beams), parabola, circle and power expansions of the Cartesian oval. Parabolic lenses reduce very much the spherical aberrations, a result that is consistent with the high popularity of these lenses. However, elliptical lenses should be preferred to parabolic lenses for nanofocusing, in particular for large lens apertures. The major differences are not on the FWHM spot size but in the intensity of the tails and therefore in the peak intensity (related to gain). The results of the simulations presented suggest that, for highly demagnifying optics, it could be beneficial to use lenses

with a profile that follows the Cartesian oval, to reduce the tails and obtain the ideal Gaussian focus.

The results show that the ray-tracing technique is adequate for helping in the design of X-ray lens systems. Work is in progress for the full implementation of the compound refractive lens system in the *SHADOW3* (Sanchez del Rio *et al.*, 2011) code, that will permit the simulation of arrays of ellipses or parabolas, and the full control of the interface parameters, like varying curvatures.

APPENDIX A Some consequences of Fermat’s principle

A1. Snell’s Law

Let us define a three-dimensional reference system centred at the optical element pole, with the y and x axes tangential to the lens surface at the lens pole, and the z axis along the optical axis.

Let us select $P_1 = (0, 0, z_1)$ in a non-dispersive medium with refraction index n_1 , and $P_2 = (0, y_2, z_2)$ a point in a medium with n_2 , separated by a plane interface passing through $(0, y, 0)$ and with normal along Z (Fig. 9a). The optical path from P_1 to P_2 is

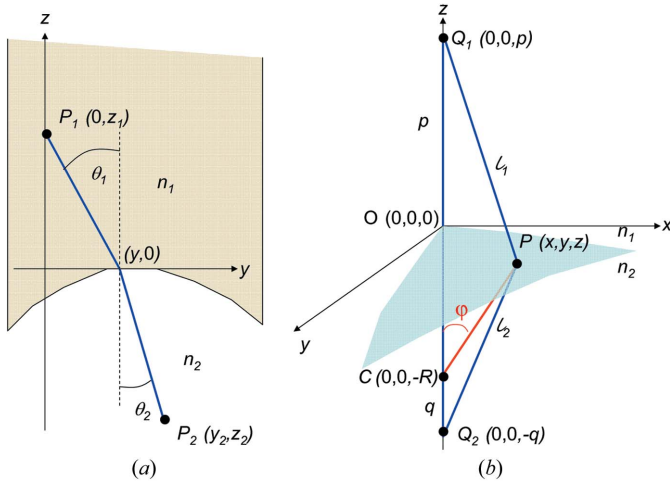


Figure 9
(a) Schematic diagram for deducing Snell's law using Fermat's principle.
(b) Three-dimensional schematic diagram of an interface that focuses a point source Q_1 at an image point Q_2 .

$$OP = n_1(y^2 + z_1^2)^{1/2} + n_2[(y_2 - y)^2 + z_2^2]^{1/2}. \quad (13)$$

The principle of Fermat requires that the trajectory of the light from P_1 to P_2 makes the OP stationary, thus

$$\frac{\partial OP}{\partial y} = 0 = n_1 \frac{y}{(y^2 + z_1^2)^{1/2}} - n_2 \frac{(y_2 - y)}{[(y_2 - y)^2 + z_2^2]^{1/2}}, \quad (14)$$

which implies

$$n_1 \sin \theta_1 = n_2 \sin \theta_2. \quad (15)$$

A2. Radius of focusing sphere

Let us define a spherical surface of radius R passing through $O = (0, 0, 0)$ with centre at $C = (0, 0, -R)$, separating two media of refraction index n_1 and n_2 (Fig. 9b). The optical path is

$$\begin{aligned} OP &= n_1 l_1 + n_2 l_2 \\ &= n_1 [R^2 + (p + R)^2 - 2R(p + R) \cos \varphi]^{1/2} \\ &\quad + n_2 [R^2 + (q - R)^2 + 2R(q - R) \cos \varphi]^{1/2}, \end{aligned} \quad (16)$$

where the cosine theorem has been applied in the triangles Q_1CP and PCQ_2 .

Applying Fermat's principle with respect to φ we obtain

$$\begin{aligned} \frac{\partial OP}{\partial \varphi} = 0 &= n_1 \frac{R(p + R) \sin \varphi}{[R^2 + (p + R)^2 - 2R(p + R) \cos \varphi]^{1/2}} \\ &\quad + n_2 \frac{R(q - R) \sin \varphi}{[R^2 + (q - R)^2 + 2R(q - R) \cos \varphi]^{1/2}}. \end{aligned} \quad (17)$$

This equation does not have a general solution for any value of φ . Expanding on a first-order power series around $\varphi = 0$, we obtain

$$\frac{\partial OP}{\partial \varphi} = 0 = \left[n_1 \frac{R(p + R)}{p} + n_2 \frac{R(q - R)}{q} \right] \varphi + O(\varphi^2), \quad (18)$$

which gives the equation of the radius of curvature R for focusing under first-order paraxial or Gaussian optics (*i.e.* the angle formed by the incident and refracted beams is very small with respect to the optical axis, which passes closer to the centre of the surface),

$$\frac{n_1}{p} + \frac{n_2}{q} = \frac{n_2 - n_1}{R}. \quad (19)$$

A3. Cartesian oval

Let us define a generic point P on the lens surface, and the source (image) point Q_1 (Q_2) as defined in Fig. 9(b). Fermat's principle requires that the optical path of the light through the point P and another point on the surface, *e.g.* $O = (0, 0, 0)$, are the same,

$$pn_1 + qn_2 = l_1 n_1 + l_2 n_2. \quad (20)$$

Substituting $l_1 = [x^2 + y^2 + (z - p)^2]^{1/2}$ and $l_2 = [x^2 + y^2 + (z + q)^2]^{1/2}$ and expanding the expression, one arrives at a particular case of the bi-circular quartic equation. In the two-dimensional case ($x = 0$),

$$\sum_{i=0}^4 \sum_{j=0}^4 a_{ij} y^i z^j = 0. \quad (21)$$

The coefficient's matrix is

$$(a_{ij}) = \begin{pmatrix} 0 & a_{01} & a_{02} & a_{03} & a_{04} \\ 0 & 0 & 0 & 0 & 0 \\ a_{20} & a_{21} & a_{22} & 0 & 0 \\ 0 & 0 & 0 & 0 & 0 \\ a_{40} & 0 & 0 & 0 & 0 \end{pmatrix}, \quad (22)$$

where

$$\begin{aligned} a_{01} &= \frac{8n_1 n_2 p q (n_1 p + n_2 q)}{(n_1 - n_2)(n_1 + n_2)^2}, \\ a_{02} &= \frac{4n_1^2 p^2 (n_1 + n_2) - 4n_2^2 q^2 (n_1 + n_2) + 4n_1 n_2 p q (n_2 - n_1)}{(n_1 - n_2)(n_1 + n_2)^2}, \\ a_{03} &= -\frac{4(n_1^2 p + n_2^2 q)}{n_1^2 - n_2^2}, \\ a_{04} &= 1, \\ a_{20} &= -\frac{4n_1 n_2 (n_1 q + n_2 p)(n_1 p + n_2 q)}{(n_1^2 - n_2^2)^2}, \\ a_{21} &= -\frac{4(n_1^2 p + n_2^2 q)}{n_1^2 - n_2^2}, \\ a_{22} &= 2, \\ a_{40} &= 1. \end{aligned} \quad (23)$$

For the three-dimensional case, where the lens has cylindrical symmetry around Z , the expression corresponding to (21) is obtained by replacing y with $[x^2 + y^2]^{1/2}$.

References

- Alianelli, L., Sawhney, K. J. S., Tiwari, M. K., Dolbnya, I. P., Stevens, R., Jenkins, D. W. K., Loader, I. M., Wilson, M. C. & Malik, A. (2009). *J. Synchrotron Rad.* **16**, 325–329.

- Aristov, V., Grigoriev, M., Kuznetsov, S., Shabelnikov, L., Yunkin, V., Weitkamp, T., Rau, C., Snigireva, I., Snigirev, A., Hoffmann, M. & Voges, E. (2000). *Appl. Phys. Lett.* **77**, 4058–4060.
- Barkla, C. G. (1916). *Philos. Mag.* **31**, 257–260.
- Cerrina, F. & Sanchez del Rio, M. (2010). *Ray-Tracing of X-ray Optical Systems*, Vol. V, *Handbook of Optics*, 3rd ed., edited by M. Bass. New York: McGraw Hill.
- Debart, P. (2011). *Ovales de Descartes*, <http://debart.pagesperso-orange.fr/geometrie/ovale.html>.
- Descartes, R. (1637). *La Géométrie*, p. 352.
- Evans-Lutterodt, K., Ablett, J., Stein, A., Kao, C. C., Tennant, D., Klemens, F., Taylor, A., Jacobsen, C., Gammel, P., Huggins, H., Bogart, G., Ustin, S. & Ocola, L. (2003). *Opt. Express*, **11**, 919–926.
- Evans-Lutterodt, K., Stein, A., Ablett, J. M., Bozovic, N., Taylor, A. & Tennant, D. M. (2007). *Phys. Rev. Lett.* **99**, 134801.
- Feynman, R. P. (1963). *The Feynman Lectures on Physics*. Reading: Addison-Wesley.
- Hecht, E. (1987). *Optics*, 2nd ed. Reading: Addison-Wesley.
- Herzberger, M. (1958). *Modern Geometrical Optics*. New York: Interscience.
- Lengeler, B., Schroer, C. G., Richwin, M., Tümmeler, J., Drakopoulos, M., Snigirev, A. & Snigireva, I. (1999). *Appl. Phys. Lett.* **74**, 3924–3926.
- Lengeler, B., Schroer, C., Tümmeler, J., Benner, B., Richwin, M., Snigirev, A., Snigireva, I. & Drakopoulos, M. (1999). *J. Synchrotron Rad.* **6**, 1153–1167.
- Lengeler, B., Tümmeler, J., Snigirev, A., Snigireva, I. & Raven, C. (1998). *J. Appl. Phys.* **84**, 5855–5861.
- Luneburg, R. K. (1964). *Mathematical Theory of Optics*. Berkeley: University of California Press.
- Mahajan, V. N. (1998). *Optical Imaging and Aberrations*, Part I, *Ray Geometrical Optics*. Bellingham: SPIE Optical Engineering Press.
- Rashed, R. (1990). *Isis*, **81**, 464–491.
- Sanchez del Rio, M., Canestrari, N., Jiang, F. & Cerrina, F. (2011). *J. Synchrotron Rad.* **18**, 708–716.
- Schroer, C. G., Kurapova, O., Patommel, J., Boye, P., Feldkamp, J., Lengeler, B., Burghammer, M., Riekel, C., Vincze, L., van der Hart, A. & Kuchler, M. (2005). *Appl. Phys. Lett.* **87**, 124103.
- Schroer, C. G. & Lengeler, B. (2005). *Phys. Rev. Lett.* **94**, 054802.
- Snigirev, A., Kohn, V., Snigireva, I. & Lengeler, B. (1996). *Nature (London)*, **384**, 49–51.
- Suehiro, S., Miyaji, H. & Hayashi, H. (1991). *Nature (London)*, **352**, 385–386.
- Zghal, M., Bouali, H.-E., Lakhdar, Z. B. & Hamam, H. (2007). *Proceedings of the Education and Training in Optics and Photonics Conference (ETOP) 2007* (<http://spie.org/etop/etop2007.html>).